nature photonics

ARTICLES

PUBLISHED ONLINE: 5 MAY 2013 | DOI: 10.1038/NPHOTON.2013.80

Efficient inorganic–organic hybrid heterojunction solar cells containing perovskite compound and polymeric hole conductors

Jin Hyuck Heo[1†], Sang Hyuk Im[1,2†], Jun Hong Noh[1†], Tarak N. Mandal[1], Choong-Sun Lim[1], Jeong Ah Chang[1], Yong Hui Lee[1], Hi-jung Kim[1], Arpita Sarkar[1], Md. K. Nazeeruddin[3], Michael Grätzel[3]* and Sang Il Seok[1,4]*

Inorganic–organic hybrid structures have become innovative alternatives for next-generation dye-sensitized solar cells, because they combine the advantages of both systems. Here, we introduce a layered sandwich-type architecture, the core of which comprises a bicontinuous three-dimensional nanocomposite of mesoporous (mp)-TiO_2, with $CH_3NH_3PbI_3$ perovskite as light harvester, as well as a polymeric hole conductor. This platform creates new opportunities for the development of low-cost, solution-processed, high-efficiency solar cells. The use of a polymeric hole conductor, especially poly-triarylamine, substantially improves the open-circuit voltage V_{oc} and fill factor of the cells. Solar cells based on these inorganic–organic hybrids exhibit a short-circuit current density J_{sc} of 16.5 mA cm^{-2}, V_{oc} of 0.997 V and fill factor of 0.727, yielding a power conversion efficiency of 12.0% under standard AM 1.5 conditions.

The Sun provides a reliable, sustainable and long-term supply of energy, in contrast to conventional resources such as coal and fossil fuels, and can therefore help to solve the growing global need for energy. One effective method of converting solar energy into a useful form like electricity makes use of solar cells and is based on the photovoltaic effect. Single-junction crystalline materials such as silicon and gallium arsenide, as well as other compound semiconductors, have been reported to achieve power conversion efficiencies (PCEs) of up to nearly 30% (ref. 1). However, current single-crystalline-based solar cells have limited use at large scales, because the manufacturing costs of photovoltaic cells are still relatively high. The development of new solar cell technologies with lower production costs (through the use of economical and abundant materials and inexpensive processes) is therefore of great interest to industry.

The mesoscopic (or nanoscale) dye-sensitized solar cell (DSC), invented by Michael Grätzel and Brian O'Regan in 1991 (ref. 2), is an attractive alternative to existing solid-state p–n junction solar cells. DSCs with photoelectric conversion efficiencies of over 12% have been achieved using a liquid electrolyte[3], and have potential in renewable electricity generation. Excellent stability data have been obtained for liquid DSCs, but much less is known about the stability of solid-state DSCs. A volatile electrolyte will cause potential problems on sealing the device, although efficient sealant materials have now been developed for DSCs. Accordingly, p-type inorganic semiconductors[4] or organic hole-transport materials (HTMs)[5,6] have been investigated, together with solvent-free polymer electrolytes, as potential substitutes for liquid electrolytes. However, fully solid-state DSCs are less efficient than liquid-type DSCs, although Kanatzidis's group recently achieved a PCE of 8.5% with a solid-state DSC by using the p-type inorganic semiconductor $CsSnI_3$ as the HTM[4]. The use of inorganic semiconductors such as quantum dots as sensitizers in DSCs, in place of metal complexes or organic dyes, may be advantageous because of their excellent optical properties[7], high extinction coefficients[8] and large intrinsic dipole moments[9]. Nevertheless, although considerable progress has been made in improving the PCEs of fully solid-state semiconductor-sensitized solar cells[10–13], these cells still suffer from low performance, mainly because of rapid carrier recombination at the various device interfaces[14]. Recently, inorganic–organic lead halide perovskite compounds have been used as the sensitizer in a DSC, but the stability of such cells, particularly in the presence of the I^-/I_3^- electrolyte, was poor[15,16].

Motivated by the goal of fabricating stable, high-efficiency and cost-effective solid-state solar cells, we studied the performance of inorganic–organic heterojunction solar cells fabricated using inorganic–organic perovskite compounds ($CH_3NH_3PbI_3$) as light harvesters on mesoporous (mp)-TiO_2, and poly-3-hexylthiophene (P3HT), poly-[2,1,3-benzothiadiazole-4,7-diyl[4,4-bis(2-ethylhexyl)-4H-cyclopenta[2,1-*b*:3,4-*b*′]dithiophene-2,6-diyl]] (PCPDTBT), (poly-[[9-(1-octylnonyl)-9H-carbazole-2,7-diyl]-2,5-thiophenediyl-2,1,3-benzothiadiazole-4,7-diyl-2,5-thiophenediyl]) (PCDTBT) and poly-triarylamine (PTAA) as HTMs or electron-blocking layers. The cells performed remarkably well, with an incident photon-to-current efficiency (IPCE) of ~71% at a wavelength of 500 nm and a maximum PCE of 12.0% under AM 1.5G illumination at an intensity of 100 mW cm^{-2} when PTAA was used as the HTM. For comparison, we also measured the performance of cells fabricated under the same conditions but using the small molecular hole conductor 2,2,7,7-tetrakis-(*N*,*N*-di-*p*-methoxyphenylamine) 9,9-bifluorene (spiro-OMeTAD) instead of the polymeric HTMs. The latter studies were motivated by reports (which emerged during

[1]Division of Advanced Materials, Korea Research Institute of Chemical Technology, 141 Gajeong-Ro, Yuseong-Gu, Daejeon 305-600, Korea, [2]Department of Chemical Engineering, Kyung Hee University, 1 Seochon-dong, Giheung-gu, Youngin-si, Gyeonggi-do 446-701, Korea, [3]Laboratory for Photonics and Interfaces, Institute of Chemical Sciences and Engineering, School of Basic Science, Swiss Federal Institute of Technology, CH-1015 Lausanne, Switzerland, [4]Department of Energy Science, Sungkyunkwan University, Suwon 440-746, Korea, †These authors contributed equally to this work. *e-mail: seoksi@krict.re.kr; michael.graetzel@epfl.ch

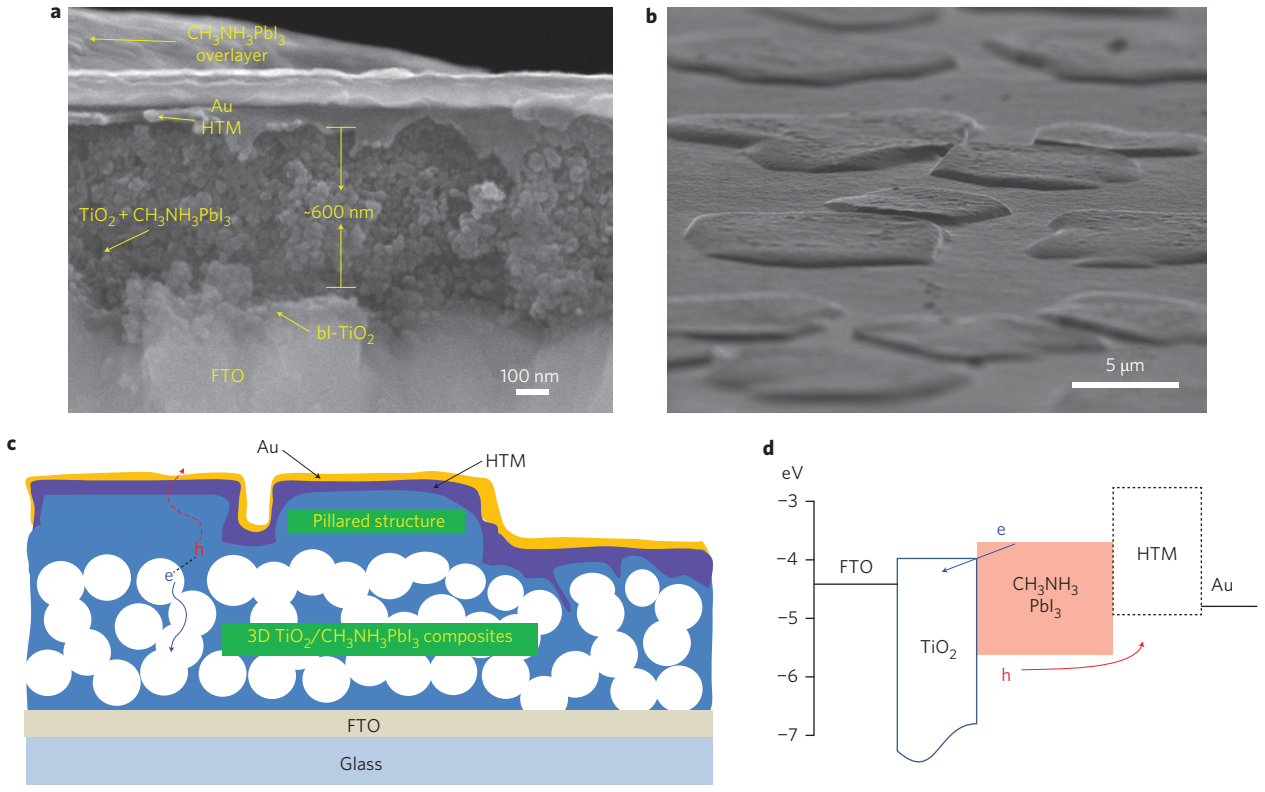

Figure 1 | SEM images, general scheme and energy level diagram of a cell. a, SEM cross-sectional image of inorganic–organic hybrid heterojunction solar cell. **b**, SEM surface image of $CH_3NH_3PbI_3$-coated mp-TiO_2 film. **c**, Schematic of device architecture. **d**, Energy levels for TiO_2, $CH_3NH_3PbI_3$ and the HTM.

the review process for this Article) relating to the successful application of spiro-OMeTAD to mesoscopic cells using $CH_3NH_3PbI_3$ (ref. 17) and $CH_3NH_3PbI_2Cl$ (ref. 18) as light harvesters. Here, we propose a new platform that includes a three-dimensional nanocomposite and bilayer architecture with an inorganic–organic hybrid heterojunction, and report that mp-TiO_2/$CH_3NH_3PbI_3$/polymeric HTMs/Au can be used to fabricate greatly improved all-solid-state solar cells using a simple solution process.

The metal-halide-based perovskite compounds with the general formula $(RNH_3)MX_3$ (R = C_nH_{2n+1}; X = halogen I, Br, Cl; M = Pb, Cd, Sn and so on) that were used in this study as light harvesters are typical self-assembled materials[19]. The $CH_3NH_3PbI_3$, prepared by drying 40 wt% of $CH_3NH_3PbI_3$/γ-butyrolactone solution at 100 °C, was characterized by X-ray diffraction (XRD) and thermogravimetric analysis (TGA) (Supplementary Fig. S1). Strong peaks at 14.08, 14.19, 28.24 and 28.50°, corresponding to the (002), (110), (004) and (220) planes, confirm the formation of a tetragonal perovskite structure with lattice parameters of $a = b = 8.88$ Å and $c = 12.68$ Å (the inset in Supplementary Fig. S1 shows the schematic crystal structure of perovskite). The TGA spectrum shows that the perovskite crystal is thermally stable up to 300 °C, but quickly decomposes above this temperature due to the decomposition of the CH_3NH_3I component, the weight fraction of which is 25.6% in $CH_3NH_3PbI_3$.

Figure 1a presents a cross-sectional scanning electron microscopy (SEM) image of a representative solar cell device. Apparently, the pores of the mp-TiO_2 film are infiltrated with $CH_3NH_3PbI_3$ perovskite, and overlayers of $CH_3NH_3PbI_3$ co-exist on top of the mp-TiO_2 film. Figure 1b shows a tilted SEM image of these $CH_3NH_3PbI_3$ overlayers on the mp-TiO_2 film covered with Au/PTAA. This image shows that several micrometre-sized $CH_3NH_3PbI_3$ islands are densely formed on the mp-TiO_2 film. It is crucial to determine the filling fraction and infiltration depth of the $CH_3NH_3PbI_3$ and HTMs into the mp-TiO_2, because these factors indicate whether the $CH_3NH_3PbI_3$ nanocrystals are contacted by the HTM, as is the case for molecular sensitizers in conventional solid-state DSCs. Measurements were performed for a representative fluorine-doped tin oxide (FTO)/TiO_2/$CH_3NH_3PbI_3$/PTAA/Au full cell using energy-dispersive X-ray spectra (EDS) mapping and X-ray photoelectron spectroscopy (XPS) depth profiling of each element, and are presented in Supplementary Fig. S2. The EDS mapping (Supplementary Fig. S3) of each element confirmed that the $CH_3NH_3PbI_3$ had infiltrated well to the bottom of the mp-TiO_2 film, with the formation of continuous phases. The mapping of elementary Pb and I showed that the $CH_3NH_3PbI_3$ was relatively more concentrated around the $CH_3NH_3PbI_3$ overlayer, and the $CH_3NH_3PbI_3$ domain was also relatively more densely interconnected in the mp-TiO_2 film, showing pillared structures. In contrast, from the XPS depth profile of elementary C in Supplementary Figs S2 or S3, PTAA was mostly located on and near the surface of the pillared structure. The peaks of I and Pb elements at early etching times (<1,000 s = 50 nm thickness) are attributed to the $CH_3NH_3PbI_3$ overlayers. Moreover, in some parts where there are no $CH_3NH_3PbI_3$ overlayers, PTAA seems to be partially infiltrated, mainly near the surface of the $TiO_2/CH_3NH_3PbI_3$ composite layer. Thus, from EDS mapping and the XPS depth profile of each element, we conclude that the pillared structure consisting of three-dimensional composites of $TiO_2/CH_3NH_3PbI_3$ (with good penetration of PTAA into parts where there are no $CH_3NH_3PbI_3$ overlayers and on the surface of the $TiO_2/CH_3NH_3PbI_3$ composite layer) appears to be key to obtaining excellent performance from the cells. This indicates that the cell configuration in our work differs considerably from that of mesoscopic cells using spiro-OMeTAD as HTM[17,18]. The main distinction is that the small molecular HTM spiro-OMeTAD can more easily infiltrate into mp-TiO_2 than can the high-molecular-weight polymer PTAA. Based on SEM, XPS and EDS analysis, we schematically drew the device architecture with a pillared structure (Fig. 1c). A noteworthy

feature of the device morphology is the small $CH_3NH_3PbI_3$ crystalline domains that are densely formed on top of the mp-TiO_2 at the first stage (by solvent-drying during spin-coating), as a result of forced convective flow towards the top layer, then further evaporation. We believe that this, together with the bicontinuous structure of the TiO_2/CH_3NH_3PbI nanocomposite, is effective in extracting the charge carriers because the short diffusion length of the excitons to the TiO_2/CH_3NH_3PbI interface renders unnecessary any displacement of the excitons over long distances. The CH_3NH_3PbI domains on top of the mesoporous TiO_2 do not appear to form a continuous and conformal coating. However, their large area of interface with the HTM overlayer assists in hole extraction to the gold electrode.

Figure 1d presents the energy band diagram of the device. The exact energy levels for TiO_2, $CH_3NH_3PbI_3$ and the hole-conducting materials used in this work are provided in Supplementary Fig. S4 (using previously reported values). Following illumination, the $CH_3NH_3PbI_3$ perovskite absorbs light to generate electron–hole pairs. The excitons dissociate mainly at the $TiO_2/CH_3NH_3PbI_3$ interface, and the remaining holes travel across the perovskite layer before reaching the hole-transporting layer. To support this, we first measured the charge transport properties of $CH_3NH_3PbI_3$ by fabricating a thin film transistor (TFT) device. As can be seen in Supplementary Fig. S5, the $CH_3NH_3PbI_3$ exhibits an ambipolar character, with a predominantly p-type behaviour. We propose that the ambipolar charge transport of $CH_3NH_3PbI_3$ plays an important role in this intriguing photovoltaic system. It enables the $CH_3NH_3PbI_3$ to act as both n- and p-type conductors, depending on the type of junction formed with the neighbouring semiconductor. It is therefore possible to separate the charges at both the $TiO_2/CH_3NH_3PbI_3$ and $CH_3NH_3PbI_3$/HTM interfaces. However, it appears that in the present cell embodiment, excitons produced by excitation of $CH_3NH_3PbI_3$ dissociate mainly at the $TiO_2/CH_3NH_3PbI_3$ interface via electron injection into the conduction band of TiO_2, and that the $CH_3NH_3PbI_3$ itself functions as a hole conductor. Unambiguous evidence for the fact that $CH_3NH_3PbI_3$ can assume a double role as light harvester and hole conductor was recently obtained from a study of mesoscopic $TiO_2/CH_3NH_3PbI_3$ heterojunction solar cells[20]. A similar device, in which a $CuInS_2$ layer produced by atomic layer deposition on a mesoporous TiO_2 film acted as both light harvester and hole conductor, has previously been reported by Nanu and colleagues[21].

To gain better insight into the mechanism that is operative during the charge separation process, we compared the photoluminescence spectra (Supplementary Fig. S6) of films composed of mp-$TiO_2/CH_3NH_3PbI_3$, mp-$TiO_2/CH_3NH_3PbI_3$/PTAA, mp-$Al_2O_3/CH_3NH_3PbI_3$ and mp-$Al_2O_3/CH_3NH_3PbI_3$/PTAA. It is well known that the electrons photogenerated in $CH_3NH_3PbI_3$ cannot be injected into Al_2O_3 due to the mismatch in energy level between the conduction band of Al_2O_3 and $CH_3NH_3PbI_3$. The slightly depressed photoluminescence spectrum of mp-$Al_2O_3/CH_3NH_3PbI_3$/PTAA indicates that a small portion of the charge carriers generated in $CH_3NH_3PbI_3$ could be separated at the $CH_3NH_3PbI_3$/PTAA interface. On the other hand, the mp-$TiO_2/CH_3NH_3PbI_3$ sample exhibited a substantial quenching of the photoluminescence spectrum, supporting the notion that the charge carriers generated in $CH_3NH_3PbI_3$ are mainly separated at the mp-$TiO_2/CH_3NH_3PbI_3$ interface. This is further supported by the fact that no additional photoluminescence quenching occurs in the mp-$TiO_2/CH_3NH_3PbI_3$/PTAA sample, which also confirms that the generated charge carriers are separated at the mp-$TiO_2/CH_3NH_3PbI_3$ interface.

Figure 2a presents photocurrent density–voltage (J–V) curves for the cells fabricated with and without P3HT, PCPDTBT, PCDTBT and PTAA as the HTM. All device performances are summarized in Table 1. The J–V curves exhibit better performance (9.0%) with PTAA than the hole-transporting polymers with thiophene groups. The superior performance obtained with PTAA may be rationalized in terms of a stronger interaction of the perovskite with PTAA compared to the other polymers. Similar behaviour has also been observed for Sb_2S_3 as light harvester and polythiophene HTMs[12]. However, further studies are needed to confirm the specific chemical interaction between PTAA and $CH_3NH_3PbI_3$, and to quantify the extent of this effect for the different polymer hole-conducting materials. An advantage of PTAA is its higher hole mobility ($\sim 1 \times 10^{-2}$ to $\sim 1 \times 10^{-3}$ $cm^2\ V^{-1}\ s^{-1}$)[22] compared to those of the other polymers ($\sim 1 \times 10^{-4}$ $cm^2\ V^{-1}\ s^{-1}$)[23–25]. Among the thiophene hole-transporting layers, the P3HT sample exhibits the best device performance, yielding 6.7% PCE under 1 sun illumination. Note that the V_{oc} of thiophene-based devices gradually increases in the order P3HT (0.73 V) → PCPDTBT (0.77 V) → PCDTBT (0.92 V), which matches the trends in the highest occupied molecular orbital (HOMO) energy level of these hole-transporting polymers (P3HT = −5.2 eV[26], PCPDTBT = −5.3 eV[27], PCDTBT = −5.45 eV[25]). As can also be seen in Fig. 2a, the J–V curve for the cell fabricated without a hole-transporting layer (that is, an FTO/bl-TiO_2/mp-$TiO_2/CH_3NH_3PbI_3$/Au device) exhibited relatively good performance, even though its performance is inferior to the other devices due to the decrease in short-circuit current density J_{sc}, open-circuit voltage V_{oc} and fill factor (FF). This confirms that photogeneration of charge carriers occurs at the mesoscopic and bicontinuous $TiO_2/CH_3NH_3PbI_3$ heterojunction[20]. The reason for the mp-$TiO_2/CH_3NH_3PbI_3$/Au device operating relatively well without an HTM may be linked to the predominantly p-type character of $CH_3NH_3PbI_3$, as explained above. Nevertheless, the performance of the device is greatly improved by the HTM. The layered sandwich-type architecture, comprising a bicontinuous three-dimensional nanocomposite of mp-TiO_2 with $CH_3NH_3PbI_3$ perovskite as light harvester, contacted on the front and back sides by a compact layer of TiO_2 and PTAA as polymer hole conductor, exhibited the best performance and hence was subjected to further scrutiny.

For mesoscopic solid-state DSCs, device performance is strongly dependent on the thickness of the mp-TiO_2 film due to effects from pore filling, light harvesting and charge carrier collection. We therefore explored the effect of the thickness of the mp-TiO_2 electrode for the present embodiment while maintaining the other experimental conditions constant. Figure 2b shows the J–V curve data for various thicknesses. The 600-nm-thick mesoporous TiO_2 film exhibited the highest PCE of 9.1%, while the 0 nm and 1,000 nm layers yielded PCE values of 0.4% and 4.2% (Table 2), respectively. The slightly lower efficiency for the 600-nm-thick mp-TiO_2 layer compared to the device shown in Fig. 2a arises from the difference in their fill factors. The three samples showed similar diffuse reflectance (Fig. 2c) and the IPCE spectra correlate well with the J_{sc} values, as shown in Fig. 2d.

The effect of mp-TiO_2 film thickness on the morphology of the $CH_3NH_3PbI_3$ overlayer on top of the mp-TiO_2 film was compared using SEM images (Supplementary Fig. S7). The $CH_3NH_3PbI_3$ island thickness decreased with increasing mp-TiO_2 layer, with the 0 nm, 600 nm and 1,000 nm TiO_2 films yielding overlayers of 500–1,000 nm, 200–300 nm and 80–100 nm thickness, respectively. Thus, the net thickness of $CH_3NH_3PbI_3$ seems to be similar for all three samples, thereby explaining the similarity of their reflectance spectra. From these morphological differences, we can surmise that the poor device performance of the device with only the compact TiO_2 layer can be attributed to the large thickness of the $CH_3NH_3PbI_3$ overlayer. The generated charge carriers in the perovskite may not be effectively collected from the thick $CH_3NH_3PbI_3$ layer because of recombination. In addition, the excitons produced in the thick $CH_3NH_3PbI_3$ may not reach the interface area with the compact blocking layer (bl) TiO_2 before deactivation occurs. On the

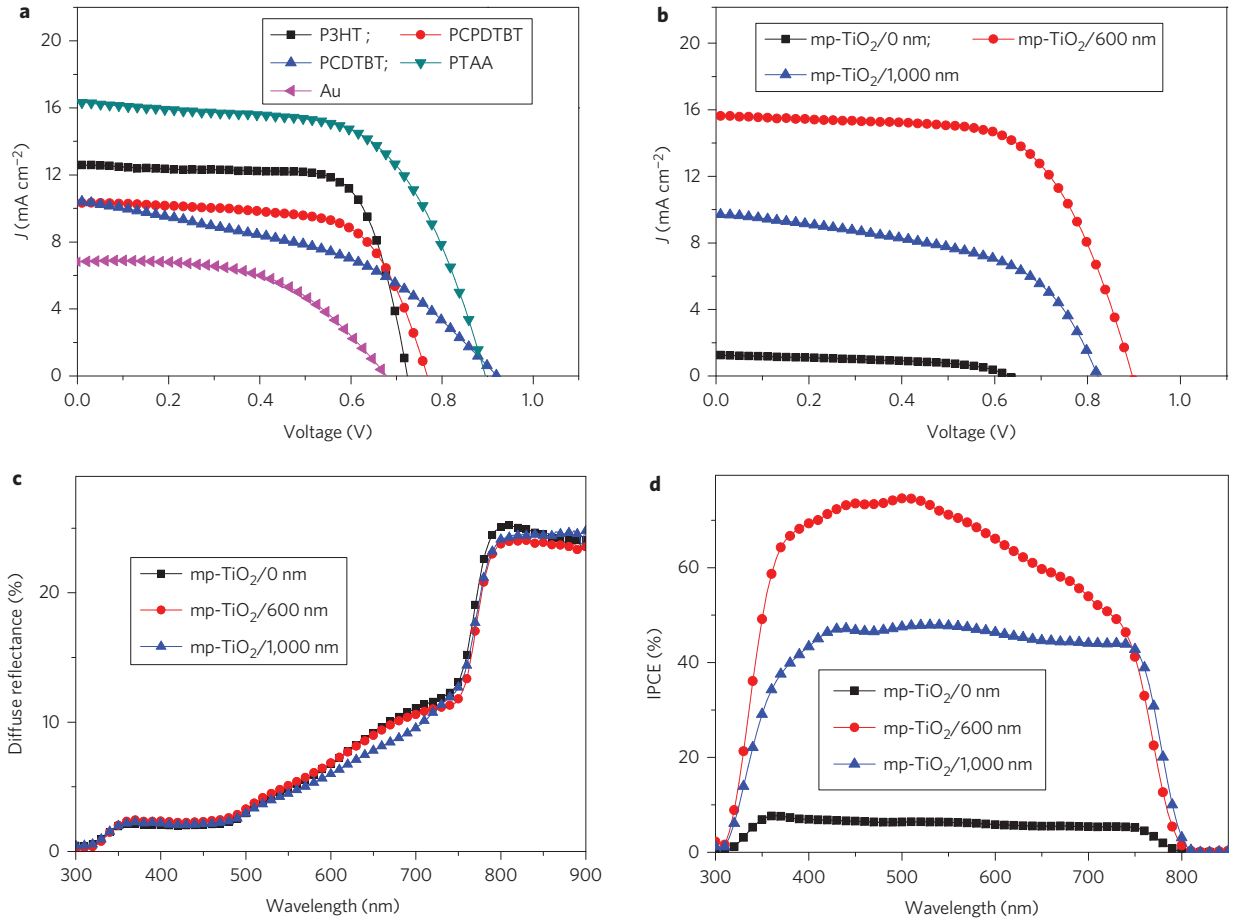

Figure 2 | *J–V*, diffuse reflectance and IPCE characteristics. a, *J–V* curves of inorganic–organic hybrid heterojunction solar cells with different hole-transporting layers (mp-TiO_2 = 1 μm). **b**, *J–V* curves of inorganic–organic hybrid heterojunction solar cells with different thicknesses of mp-TiO_2 film. **c**, Diffuse reflectance spectra of FTO/bl-TiO_2/mp-TiO_2/$CH_3NH_3PbI_3$/Au cells with different thicknesses of mp-TiO_2 film. **d**, IPCE spectra of inorganic–organic hybrid heterojunction solar cells with different thicknesses of mp-TiO_2 film.

Table 1 | Summary of device parameters obtained from FTO/bl-TiO_2/mp-TiO_2/$CH_3NH_3PbI_3$/HTM/Au (Fig. 2a).

HTM	J_{sc} (mA cm^{-2})	V_{oc} (V)	FF (%)	PCE, η (%)
P3HT	12.6	0.73	73.2	6.7
PCPDTBT	10.3	0.77	66.7	5.3
PCDTBT	10.5	0.92	43.7	4.2
PTAA	16.4	0.90	61.4	9.0
Without	6.8	0.68	53.8	2.5

Table 2 | Summary of device parameters obtained from FTO/bl-TiO_2/0-, 600- and 1,000-nm-thick mp-TiO_2/$CH_3NH_3PbI_3$/PTAA/Au (Fig. 2b).

Thickness of mp-TiO_2 (nm)	J_{sc} (mA cm^{-2})	V_{oc} (V)	FF (%)	PCE, η (%)
0	1.3	0.63	49.1	0.4
600	15.6	0.90	64.5	9.1
1,000	9.7	0.82	53.3	4.2

other hand, the 1,000 nm TiO_2 sample has a sufficient TiO_2/$CH_3NH_3PbI_3$ interface area to enable suitable charge injection from $CH_3NH_3PbI_3$ to TiO_2. However, the photogenerated holes will have to travel over a relatively longer pathway (1,000 nm + (80–100 nm)) than in the 600 nm sample (600 nm + (200–300 nm)) before reaching the HTM. At the same time, the extended interface area enhances the probability of recombination between electrons in the TiO_2 and holes in the $CH_3NH_3PbI_3$. Accordingly, the 600 nm TiO_2 sample exhibits the highest PCE due to the optimal tradeoff between TiO_2/$CH_3NH_3PbI_3$ interface area and hole path length.

Figure 3a presents a comparison of *J–V* curves for the best cells fabricated from mp-TiO_2/$CH_3NH_3PbI_3$/PTAA/Au and TiO_2/$CH_3NH_3PbI_3$/spiro-OMeTAD/Au by fixing the optimum conditions for several experimental parameters, as already discussed. We used a ~600-nm-thick mp-TiO_2 with a 40 wt% solution of $CH_3NH_3PbI_3$ in butyrolactone, 15 mg of PTAA in 1 ml of toluene and 180 mg of spiro-OMeTAD in 1 ml of dichlorobenzene, respectively. The device performance for two cells is summarized in Supplementary Table S1, together with HOMO energy level, charge mobility, series resistance and overlayer thickness between the HTM and gold. The best device, with PTAA, exhibits J_{sc} = 16.5 mA cm^{-2}, V_{oc} = 0.997 V and FF = 72.7%, corresponding to PCE = 12.0%, whereas the device with spiro-OMeTAD shows J_{sc} = 16.7 mA cm^{-2}, V_{oc} = 0.855 V and FF = 58.8%, yielding PCE = 8.4% under standard AM 1.5 reporting conditions. From a simple comparison of both devices, we see that the mp-TiO_2/$CH_3NH_3PbI_3$/PTAA-based device shows a better FF and V_{oc} than that using spiro-OMeTAD, while the J_{sc} values are similar. The *J–V* curve for V_{oc} = −0.5 V to 1.5 V for one of the cells fabricated from PTAA is presented in Supplementary Fig. S8. This allowed us to evaluate electrical properties such as series resistance, shunt resistance, and so on. The series resistance for the devices was determined

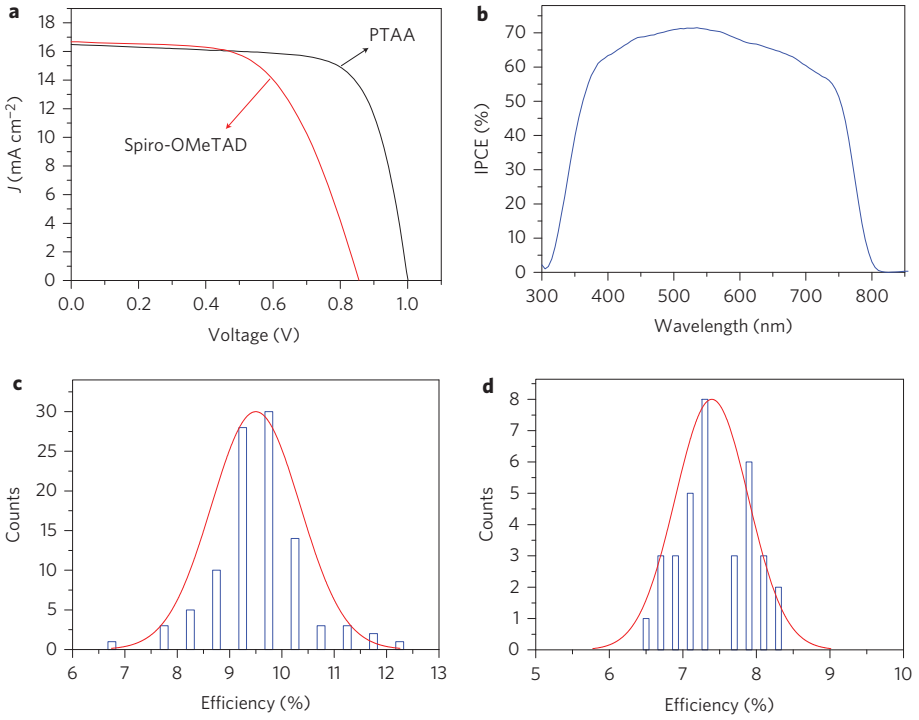

Figure 3 | *J–V* and IPCE characteristics for the best cells, and reproducibility. a, *J–V* curve for the best cells fabricated from 600-nm-thick mp-TiO_2/$CH_3NH_3PbI_3$/PTAA or spiro-OMeTAD/Au. **b**, IPCE spectrum for the best cell of 600-nm-thick mp-TiO_2/$CH_3NH_3PbI_3$/PTAA/Au. **c**, Histogram of solar cell efficiency of 100 samples from 600-nm-thick mp-TiO_2/$CH_3NH_3PbI_3$/PTAA/Au. **d**, Histogram of solar cell efficiencies for 34 samples of 600-nm-thick mp-TiO_2/$CH_3NH_3PbI_3$/spiro-OMeTAD/Au.

by fitting the *J–V* curve to an ideal diode model. Notably, we see in Supplementary Table S1 that the series resistance for PTAA (5.4 Ω cm^2) is greatly reduced compared with that of spiro-OMeTAD (12.7 Ω cm^2). The main impact of a rising series resistance is to reduce FF, although series resistance does not affect V_{oc}. The increased V_{oc} in PTAA arises mainly from the larger workfunction of PTAA. Accordingly, the improved performance for PTAA mainly stems from the increased values of FF and V_{oc}. Figure 3b presents the monochromatic IPCE spectrum for the best cell fabricated from the mp-TiO_2/$CH_3NH_3PbI_3$/PTAA/Au system, and the integrated photocurrent density is 16.4 mA cm^{-2}. Thus, the J_{sc} is well matched with the IPCE spectrum, indicating that there is hardly any spectral mismatch between the simulator used as light source and solar emission. To check the reproducibility of performance, we repeated the fabrication of the cells. As shown in Fig. 3c, ∼80% of the cells including PTAA exceed 9% in overall efficiency under 1 sun conditions. Of those, ∼30% have PCE > 10%. A histogram of the values of J_{sc}, V_{oc} and FF for 100 samples from 600-nm-thick mp-TiO_2/$CH_3NH_3PbI_3$/PTAA/Au is presented in Supplementary Fig. S9. On the other hand, the cells from spiro-OMeTAD show ∼7% average efficiency, and just 8.4% in the most efficient device (Fig. 3d).

In conclusion, we have demonstrated not only a new photovoltaic architecture with efficient photovoltaic performance, but also a useful model system to reveal the correlation between $CH_3NH_3PbI_3$ and the photovoltaic properties of inorganic–organic hybrid systems. Specifically, our study underlines that using three-dimensional composites of TiO_2/$CH_3NH_3PbI_3$ and complementary well-matched polymeric hole conductors is key to realizing good performance. A central finding of our investigation is that PTAA provides the highest efficiency among the polymeric HTMs examined, with higher FF and V_{oc} values than a device based on the molecular spiro-OMeTAD. The cells are highly reproducible and linearly dependent on the illuminated sun intensities, delivering maximum 12.0% PCE under full Sun illumination. These results will lead to more efficient and cost-effective mesoscopic inorganic–organic hybrid heterojunction solar cells in the future. We believe that the present findings offer a new platform for novel approaches to achieve high-efficiency and low-cost solar cells.

Methods

Solar cell fabrication. A 60-nm-thick layer of dense blocking TiO_2 (bl-TiO_2) was coated onto a F-doped SnO_2 (FTO, Pilkington, TEC8) substrate by spray pyrolysis deposition of 20 mM titanium diisopropoxide bis(acetylacetonate) (Aldrich) solution at 450 °C to prevent direct contact between the FTO and the hole-conducting layer. Mesoporous TiO_2 (mp-TiO_2) films with thicknesses of 250, 600 and 1,000 nm were screen-printed onto the bl-TiO_2/FTO substrate using the TiO_2 paste, which was prepared according to a reported method[9]. The films were calcined at 500 °C for 1 h to remove the organic part. The films were then immersed in 40 mM of $TiCl_4$ aqueous solution at 60 °C for 1 h and heat-treated at 500 °C for 30 min to improve interfacial contact with the nanocrystalline TiO_2. CH_3NH_3I, to be used as a light harvester, was synthesized by reacting 27.86 ml methylamine (40% in methanol, Junsei Chemical Co.) and 30 ml hydroiodic acid (57 wt% in water, Aldrich) in a 250 ml round-bottomed flask at 0 °C for 2 h with stirring. The precipitate was recovered by evaporation at 50 °C for 1 h. The product, methyl ammonium iodide (CH_3NH_3I), was dissolved in ethanol, recrystallized from diethyl ether, and dried at 60 °C in a vacuum oven for 24 h The synthesized CH_3NH_3I powder was mixed with PbI_2 (Aldrich) at a 1:1 mol ratio in γ-butyrolactone at 60 °C for 12 h, followed by filtering twice using a PTFF syringe filter (Whatman, 0.45 μm). The concentration of $CH_3NH_3PbI_3$ was 40 wt%. The $CH_3NH_3PbI_3$/γ-butyrolactone solution was then coated onto the mp-TiO_2/bl-TiO_2/FTO substrate by spin-coating at 2,000 r.p.m. for 60 s then at 3,000 r.p.m. for 60 s, and dried on a hot plate at 100 °C for 2 min. The P3HT, PCPDTBT and PCDTBT HTMs were purchased from 1-Material and used without further purification. The thiophene HTMs were spin-coated on $CH_3NH_3PbI_3$/mp-TiO_2/bl-TiO_2/FTO substrate at 3,000 r.p.m. for 30 s using HTMs/1,2-dichlorobenzene (15 mg/1 ml) with 6.8 μl Li-bis(trifluoromethanesulfonyl) imide (Li-TFSI)/acetonitrile (28.3 mg/1 ml) and 3.4 μl TBP as additives. A PTAA (EM index, M_w = 17,500 g mol^{-1})/toluene (15 mg/1 ml) solution with added 13.6 μl Li-bis(trifluoromethanesulfonyl) imide (Li-TFSI)/acetonitrile (28.3 mg/1 ml) and 6.8 μl TBP was spin-coated on $CH_3NH_3PbI_3$/mp-TiO_2/bl-TiO_2/FTO substrate at 3,000 r.p.m. for 30 s. As a small molecular HTM, a spiro-OMeTAD (Merck)/chlorobenzene (180 mg/1 ml)

solution was used with added 37.5 μl Li-bis(trifluoromethanesulfonyl) imide (Li-TFSI)/acetonitrile (170 mg/1 ml) and 17.5 μl TBP. Finally, a gold counterelectrode was deposited by thermal evaporation. The active area was fixed at 0.16 cm^2.

Device characterization. IPCE was measured using a power source (Newport 300 W xenon lamp, 66920) with a monochromator (Newport Cornerstone 260) and a multimeter (Keithley 2001). The current density–voltage (J–V) curves were measured with a solar simulator (Newport, Oriel Class A, 91195A) with a source meter (Keithley 2420) at 100 mA cm^{-2} illumination (AM 1.5G) and a calibrated Si-reference cell certificated by NREL. The J–V curves of all devices were measured by masking the active area with a metal mask of area 0.096 cm^2.

Received 17 July 2012; accepted 6 March 2013; published online 5 May 2013

References

1. Green, M. A., Emery, K., Hishikawa, Y., Warta, W. & Dunlop, E. D. Solar cell efficiency tables (version 39). *Prog. Photovolt. Res. Appl.* **20,** 12–20 (2012).
2. O'Regan, B. & Grätzel, M. A low-cost, high-efficiency solar cell based on dye-sensitized colloid TiO_2 films. *Nature* **353,** 737–740 (1991).
3. Yella, A. *et al.* Porphyrin-sensitized solar cells with cobalt (II/III)-based redox electrolyte exceed 12 percent efficiency. *Science* **334,** 629–634 (2011).
4. Chung, I. *et al.* All-solid-state dye-sensitized solar cells with high efficiency. *Nature* **485,** 486–489 (2012).
5. Zhang, W. *et al.* High-performance solid-state organic dye sensitized solar cells with P3HT as hole transporter. *J. Phys. Chem. C* **115,** 7038–7043 (2011).
6. Burschka, J. *et al.* Tris(2-(1H-pyrazol-1-yl)pyridine)cobalt(III) as p-type dopant for organic semiconductors and its application in highly efficient solid-state dye-sensitized solar cells. *J. Am. Chem. Soc.* **133,** 18042–18045 (2011).
7. Mora-Sero, I. & Bisquert, J. Breakthroughs in the development of semiconductor-sensitized solar cells. *J. Phys. Chem. Lett.* **1,** 3046–3052 (2010).
8. Sun, J. & Goldys, E. M. Linear absorption and molar extinction coefficients in direct semiconductor quantum dots. *J. Phys. Chem. C* **112,** 9261–9266 (2008).
9. Hanewinkel, B., Knorr, A., Thomas, P. & Koch, S. W. Optical near-field response of semiconductor quantum dots. *Phys. Rev. B* **55,** 13715–13725 (1997).
10. Chang, J. A. *et al.* High-performance nanostructured inorganic–organic heterojunction solar cells. *Nano Lett.* **10,** 2609–2612 (2010).
11. Im, S. H. *et al.* All solid state multiply layered PbS colloidal quantum-dot-sensitized photovoltaic cells. *Energy Environ. Sci.***4,** 4181–4186 (2011).
12. Im, S. H. *et al.* Toward interaction of sensitizer and functional moieties in hole-transporting materials for efficient semiconductor-sensitized solar cells. *Nano Lett.* **11,** 4789–4793 (2011).
13. Chang, J. A. *et al.* Panchromatic photon-harvesting by hole-conducting materials in inorganic–organic heterojunction sensitized-solar cell through the formation of nanostructured electron channels. *Nano Lett.* **12,** 1863–1867 (2012).
14. Boix, P. P. *et al.* From flat to nanostructured photovoltaics: balance between thickness of the absorber and charge screening in sensitized solar cells. *ACS Nano* **6,** 873–880 (2012).
15. Kojima, A., Teshima, K., Shirai, Y. & Miyasaka, T. Organometal halide perovskites as visible-light sensitizers for photovoltaic cells. *J. Am. Chem. Soc.* **131,** 6050–6051 (2009).
16. Im, J.-H. *et al.* 6.5% efficient perovskite quantum-dot-sensitized solar cell. *Nanoscale* **3,** 4088–4093 (2011).
17. Kim, H.-S. *et al.* Lead iodide perovskite sensitized all-solid-state submicron thin film mesoscopic solar cell with efficiency exceeding 9%. *Sci. Rep.* **2,** 591 (2012).
18. Lee, M. M. *et al.* Efficient hybrid solar cells based on meso-superstructured organometal halide perovskites, *Science* **338,** 643–647 (2012).
19. Ziyong Cheng, Z. & Lin, J. Layered organic–inorganic hybrid perovskites: structure, optical properties, film preparation, patterning and templating engineering. *CrystEngComm* **12,** 2646–2662 (2010).
20. Etgar, L. *et al.* Mesoscopic $CH_3NH_3PbI_3/TiO_2$ heterojunction solar cells, *J. Am. Chem. Soc.* **134,** 17396–17399 (2012).
21. Nanu, M., Schoonman, J. & Goossens, A. Nanocomposite three-dimensional solar cells obtained by chemical spray deposition. *Nano Lett.* **5,** 1716–1719 (2005).
22. Zhang, W. *et al.* Systematic improvement in charge carrier mobility of air stable triarylamine copolymers. *J. Am. Chem. Soc.* **131,** 10814–10815 (2009).
23. Ebadian, S. *et al.* Effects of annealing and degradation on regioregular polythiophene-based bulk heterojunction organic photovoltaic devices. *Sol. Energy Mater. Sol. Cells* **94,** 2258–2264 (2010).
24. Namkoong, G., Boland, P., Lee, K. & Dean, J. Design of organic tandem solar cells using PCPDTBT:PC_{61}BM and P3HT:PC_{71}BM. *J. Appl. Phys.* **107,** 124515 (2010).
25. Kim, B. *et al.* A selenophene analogue of PCDTBT: selective fine-tuning of LUMO to lower the bandgap for efficient polymer solar cells. *Macromolecules* **45,** 8658–8664 (2012).
26. Shen, L. *et al.* Performance improvement of TiO_2/P3HT solar cells using CuPc as a sensitizer. *Appl. Phys. Lett.* **92,** 073307 (2008).
27. Morana, M. *et al.* Bipolar charge transport in PCPDTBT-PCBM bulk-heterojunctions for photovoltaic applications. *Adv. Funct. Mater.* **18,** 1757–1766 (2008).

Acknowledgements

This work was supported by the Global Research Laboratory (GRL) Program, the Global Frontier R&D Program at the Center for Multiscale Energy System funded by the National Research Foundation in Korea, and by a grant from the KRICT 2020 Program for Future Technology of the Korea Research Institute of Chemical Technology (KRICT), Republic of Korea. M.G. expresses his gratitude to the European Research Council (ERC) for supporting part of this work under an advanced research grant (no. 247404, MESOLIGHT).

Author contributions

S.I.S. and S.H.I. conceived the experiments, carried out data analysis and prepared the manuscript. M.G. and M.K.N. contributed to the analysis of data and revision of the manuscript. J.H.H., J.H.N. and S.H.I carried out preparation of the devices and device performance measurements. T.N.M. and C.-S.L. synthesized materials for $CH_3NH_3PbI_3$ and S.I.S prepared TiO_2 pastes for the electrodes. Y.H.L., H.J.K. and A.S. prepared the mesoporous electrode. J.A.C. fabricated test specimens for comparisons. S.I.S. and M.G directed the study. All authors discussed the results and commented on the manuscript.

Additional information

Supplementary information is available in the online version of the paper. Reprints and permissions information is available online at www.nature.com/reprints. Correspondence and requests for materials should be addressed to M.G. and S.I.S.

Competing financial interests

The authors declare no competing financial interests.